CrossMark

Facile synthesis of CoNi$_2$S$_4$/graphene nanocomposites as a high-performance electrode for supercapacitors

Jingjing Lin[1] · Song Yan[1] · Ping Liu[1] · Xing Chang[1] · Lu Yao[1] ·
Hualin Lin[1] · Deli Lu[1] · Sheng Han[1]

Abstract CoNi$_2$S$_4$/graphene nanocomposites were synthesized by a simple solvothermal method and used as supercapacitor electrodes. CoNi$_2$S$_4$ nanoparticles were doped in graphene layers, which is favorable for improving electrochemical performances of the as-prepared materials. The resulting electrochemical performance of CoNi$_2$S$_4$/graphene nanocomposite electrodes possessed pseudocapacitive behavior with high specific capacitance (1621 F g^{-1} at 0.5 A g^{-1}), good rate capability (76.7% capacitance retention when reaching 10 A g^{-1}) and outstanding cycling stability (no capacitance loss after 2500 charge–discharge cycles at 5 A g^{-1}). In addition, as the positive electrode of an asymmetric supercapacitor, the material also shows a high specific capacitance of 126.6 F g^{-1} at 0.5 A g^{-1}, good cycle stability with capacitance retention of 87.4% after 5000 cycles and the highest energy density of 39.56 W h kg^{-1} at the power density of 374.8 W kg^{-1}.

✉ Deli Lu
  ldl@sit.edu.cn

✉ Sheng Han
  hansheng654321@sina.com

[1] School of Chemical and Environmental Engineering, Shanghai Institute of Technology, Haiquan Road 100, Shanghai 201418, People's Republic of China

Introduction

Supercapacitors have experienced a developing course for more than 30 years. Due to their excellent characteristics with long lifespan, strong environment adaptiveness, superior charge–discharge efficiency, high power density, flexible operating temperature and energy conservation [1–3], supercapacitors have become one of the most deserving areas of research in the world and are found in increasing numbers in many applications, such as electric vehicles, pulse laser techniques, military devices, wind energy equipment and memory storage systems [4–6].

Currently, commercial supercapacitors are, from a materials point of view, mostly made of high-surface area carbon-based and metal electrode materials. Carbonaceous materials are dominant mainly from the electric double-layer energy storage mechanism by the charge-transfer process between the electrode surface and electrolyte ions [7], such as carbon nanotubes [8], graphene [9, 10], activated carbon [11, 12], carbon nanofibers [13, 14] and organic carbide [15, 16]. Compared with other carbonaceous materials, graphene possesses intriguing properties with a unique structure, showing high electrical conductivity, good mechanical strength, high theoretical surface area and superior thermal stability [17, 18]. By virtue of adjusting ionic charges easily through electrostatic interactions, graphene can serve as a current collector which delivers electrons rapidly from charge transfer reactions of anchored pseudo-capacitive materials [19]. Many reports have proved that graphene is an excellent substrate when combined with transition metal oxides/hydroxides in supercapacitors [20–22], in which graphene-based electroactive materials offer enormous potential. Despite its superior properties with excellent cycle stability and high conductivity, graphene shows a lower capacitance and lower energy density than pseudocapacitive materials.

Metal electrode materials, such as RuO_2 and MnO_2, store energy by a pseudocapacitance effect with fast reversible Faradaic redox reactions at the multi-electron surface [7, 23] to obtain high specific capacitance, but the inherent weakness of lower electrical conductivity and poor rate performance is caused by the instability of volume. Other pseudo-capacitive electrode materials of transition metal oxides with high oxidation states, such as Co_3O_4 [24], $NiCo_2O_4$ [25] and $MnMo_2O_4$ [26], have been researched to replace RuO_2. Compared with these transition metal oxides, transition ternary metal sulfides, especially $NiCo_2S_4$ and $CoNi_2S_4$, have recently gained great attention due to their satisfactory structural features and higher efficiency electrochemical behavior in supercapacitors [27–29]. For example, $CoNi_2S_4$ shows higher electroconductivity than $CoNi_2O_4$ and is expected to provide better redox reactions than single cobalt sulfides or nickel sulfides [27]. The addition of graphene into metal materials can broaden the operating voltage window and further improve the conductivity of nanocomposites. It is thus necessary to design graphene-based metal electrode materials with electrochemical activities and microstructures.

Considering the characteristics of $CoNi_2S_4$ and graphene, we designed a novel nanocomposite called $CoNi_2S_4$/rGO, in which $CoNi_2S_4$ nanoparticles were successfully doped on graphene sheets through a simple solvothermal method. In

the $CoNi_2S_4$/rGO nanocomposites, graphene acts as the substrate for the growth of $CoNi_2S_4$ nanoparticles and can anchor pseudocapacitive nanomaterials, and in addition, it accelerates electron and ion transport of the electrode materials. $CoNi_2S_4$/rGO nanocomposites with different additions of graphene were investigated and showed different microstructures. When used as electrode materials for supercapacitora, the $CoNi_2S_4$/rGO nanocomposites exhibit excellent electrochemical performances with high specific capacitance, excellent rate performance and good cycle stability.

Experimental

Materials

Cobalt nitrate hexahydrate, $Co(NO_3)_2·6H_2O$, nickel nitrate hexahydrate, $Ni(NO_3)_2·6H_2O$, thioacetamide, CH_3CSNH_2, and anhydrous ethanol were purchased from Sinopharm Chemical Reagent (Shanghai, China), and all the chemicals reagent were of analytical grade and used without further purification. The deionized water was prepared in own laboratory.

Preparation of CoNi₂S₄/rGO nanocomposites

Graphene oxide (GO) was prepared through the modified Hummer's method [30]. The $CoNi_2S_4$/rGO nanocomposites were synthesized by a one-step solvothermal method, and the fabrication process is illustrated in Fig. 1. The details are as follows: 1 mmol $Co(NO_3)_2·6H_2O$, 2 mmol $Ni(NO_3)_2·6H_2O$ and 4 mmol
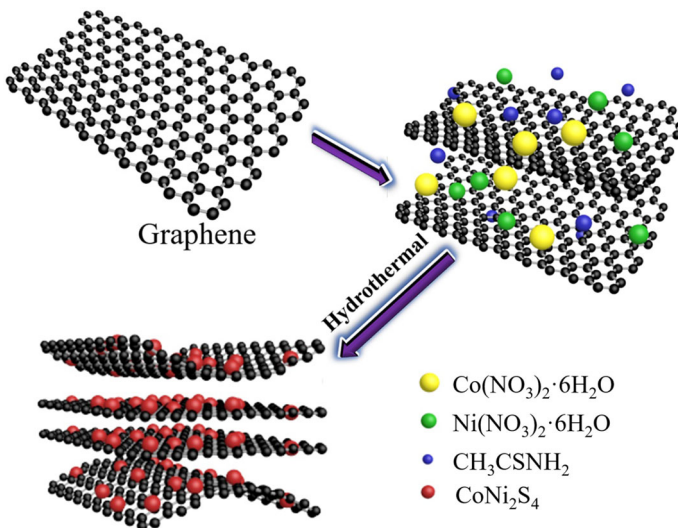

Fig. 1 Schematic of the fabrication process for CoNi₂S₄/rGO nanocomposites

CH_3CSNH_2 were dissolved in 30 mL absolute ethanol by ultrasonication. Then, GO (5 mol L^{-1}) was added into the above solution and maintained with ultrasound for 1 h to form a uniform suspension. Finally, the mixture was transferred into a Teflon-lined autoclave and maintained at 180 °C for 12 h. The obtained products were washed with water and ethanol, and freeze-dried for 72 h. The GO additions were, respectively, 30, 50 and 70 mg, and the corresponding samples were labeled $CoNi_2S_4$/rGO-1, $CoNi_2S_4$/rGO-2 and $CoNi_2S_4$/rGO-3, respectively. In addition, reduced graphene (rGO) was also obtained by a solvothermal method without the addition of $Co(NO_3)_2 \cdot 6H_2O$, $Ni(NO_3)_2 \cdot 6H_2O$ or CH_3CSNH_2.

Characterization

The morphology and structure of the obtained samples were characterized by scanning electron microscopy (SEM; Hitachi S-4800 N), and energy dispersive X-ray spectroscopy spectra (JEOL JSM 6700F). Fourier transform infrared spectroscopy (FT-IR; Bruker Vector 22) was measured at 400–4000 cm^{-1}. X-ray diffraction (XRD; PANalytical PW3040/60) was conducted with Cu Kα radiation ($\gamma = 0.1542$ nm) with the 2θ ranging from 10 to 80°. Thermal gravimetric analysis (TGA; DTG- 60AH) were carried out from 25 to 1000 °C with a heating rate of 10 °C min^{-1} in nitrogen atmosphere. Raman spectra were visulaized on a SenterraR200L multichannel confocal microspectrometer with excitation from the 532-nm line of an Ar-ion laser. Nitrogen adsorption–desorption experiments were conducted using 3H-2000PM2 at 77.3 K. An X-ray photoelectron spectra (XPS; AXIS Ultra DLD system from Kratos) was performed using an X-ray source of Al Kα radiation.

Electrochemical measurement

The electrochemical measurements of all the as-prepared samples were investigated through a three-electrode system in 2 M KOH electrolyte solution. The working electrode was fabricated as follows: active materials ($CoNi_2S_4$/rGO nanocomposites), acetylene carbon black and a binder of polytetrafluoroethylene with a mass ratio of 8:1:1 in 1.0 mL anhydrous ethanol were stirred mechanically to form a homogeneous slurry and then pressed onto a foamed nickel sheet (1 cm × 3 cm), then dried at 60 °C in a vacuum -drying oven. A platinum electrode served as the counter electrode and a Ag/AgCl electrode as the reference electrode. Cyclic voltammetry (CV), galvanostatic charge–discharge (GCD) and electrochemical impedance spectroscopy (EIS) were measured in a CHI 760E electrochemical workstation (Shanghai Chenhua, China), and the cycle behavior was determined in a LAND-CT2001A system (Wuhan, China).

Results and discussion

The morphologies of rGO, CoNi$_2$S$_4$/rGO-1, CoNi$_2$S$_4$/rGO-2 and CoNi$_2$S$_4$/rGO-3, possessing different additions of graphene, spontaneously present different CoNi$_2$S$_4$ particle sizes and graphene microstructures. As can be seen from the SEM images in Fig. 2a–f, all the CoNi$_2$S$_4$/rGO materials take on CoNi$_2$S$_4$ nanoparticles located in the graphene. The nanocomposite of CoNi$_2$S$_4$/rGO-1 (Fig. 2a, b) with less graphene turns out to have a fragile cracked piece structure and exhibits more CoNi$_2$S$_4$ nanoparticles. In addition, the CoNi$_2$S$_4$ size is not concentrated but dispersed in a broad range of 5–60 nm. Figure 2c, d depicts the morphology of CoNi$_2$S$_4$/rGO-2 at different magnifications. The whole has a three-dimensional aerogel structure and the CoNi$_2$S$_4$ nanoparticles with a concentrated size of 15–20 nm have been well
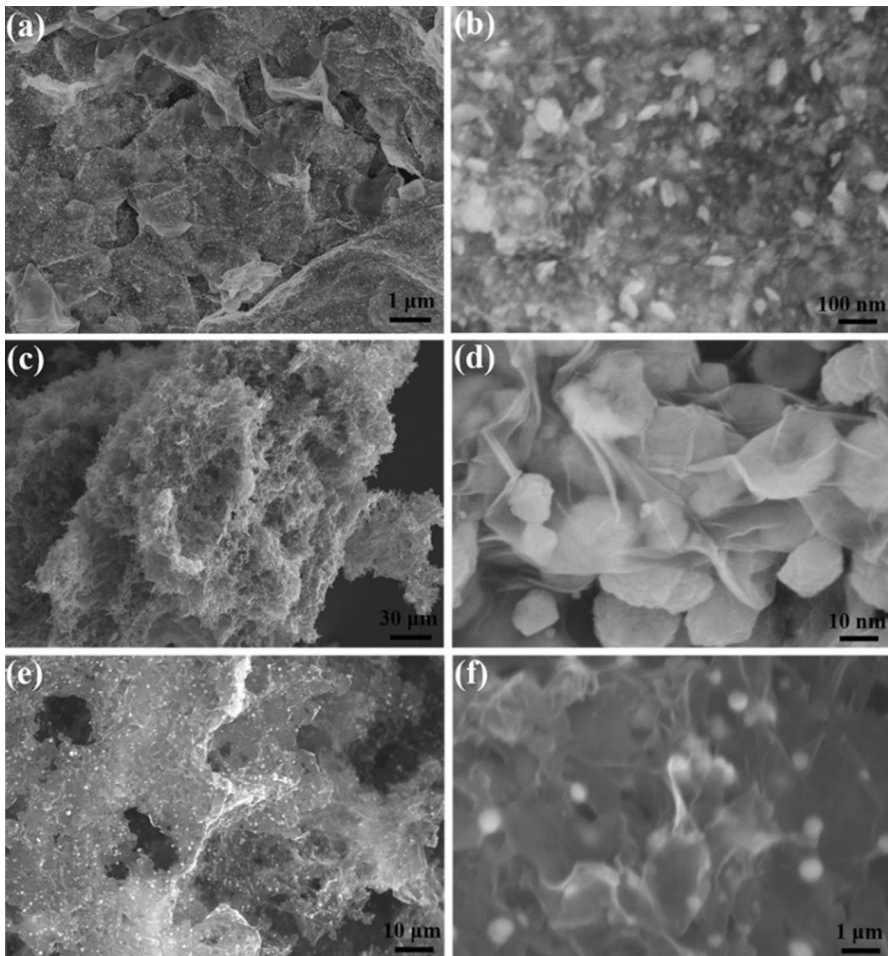

Fig. 2 SEM images: **a**, **b** CoNi$_2$S$_4$/rGO-1 nanocomposites; **c**, **d** CoNi$_2$S$_4$/rGO-2 nanocomposites; **e**, **f** CoNi$_2$S$_4$/rGO-3 nanocomposites

wrapped by the thin and wrinkled graphene layers. The well-designed three-dimensional aerogel structure implies favorable contact between the $CoNi_2S_4$ nanoparticles and the graphene layer, which is propitious for good conductivity as well as outstanding cycle stability. In addition, the three-dimensional body may provide more spaces between the graphene layer and the $CoNi_2S_4$ nanoparticles for improving the ion and electrolyte diffusion, which is crucial for further promoting the rate performance by increasing the availability of active sites in the electrode materials during the faradic redox reactions even with a high current density. As observed from the SEM images of the $CoNi_2S_4$/rGO-3 nanocomposite in Fig. 2e, f, the density of the $CoNi_2S_4$ nanoparticles in $CoNi_2S_4$/rGO-3 is significantly lower than that in $CoNi_2S_4$/rGO-1 and $CoNi_2S_4$/rGO-2. Furthermore, the $CoNi_2S_4$ size in $CoNi_2S_4$/rGO-3 has a range of 100–500 nm, obviously larger than that of $CoNi_2S_4$/rGO-1 and $CoNi_2S_4$/rGO-2.

The FT-IR spectrum has been analyzed to obtain some information about functional groups and chemical bonds of the samples. As clearly observed in Fig. 3a, the rGO exhibits several peaks within the range of 1100–1700 cm^{-1}, and the peak at about 1580 cm^{-1} is attributed to a typical C=C stretching vibration due to the sp^2 mode. and the peak located at 1370 cm^{-1} is attributed to the C–OH of graphene [31]. Moreover, the broad band at approximately 3400 cm^{-1} represents γO–H, implying the existence of rGO [21]. For $CoNi_2S_4$/rGO-1, $CoNi_2S_4$/rGO-2 and $CoNi_2S_4$/rGO-3, new peaks at 550–1100 cm^{-1} are found, which are typical peaks of $CoNi_2S_4$, demonstrating the successful formation of $CoNi_2S_4$ in the rGO layers [31].

The composition and structure of rGO, $CoNi_2S_4$/rGO-1, $CoNi_2S_4$/rGO-2 and $CoNi_2S_4$/rGO-3 have been investigated by XRD patterns, as shown in Fig. 3b. For the rGO sheets, an apparent intense peak at around 25° is well matched to the (002) plane of graphene, which can be attributed to the overlap of the graphene layers (JCPDS PDF#22-1086) [32]. For the $CoNi_2S_4$/rGO-1, $CoNi_2S_4$/rGO-2 and $CoNi_2S_4$/rGO-3 nanocomposites, the peaks exhibited at 16.06°, 26.55°, 31.60°, 38.18°, 46.73°, 50.31°, 54.42°, 59.21°, 61.72° and 77.20° corresponding to the (111), (220),

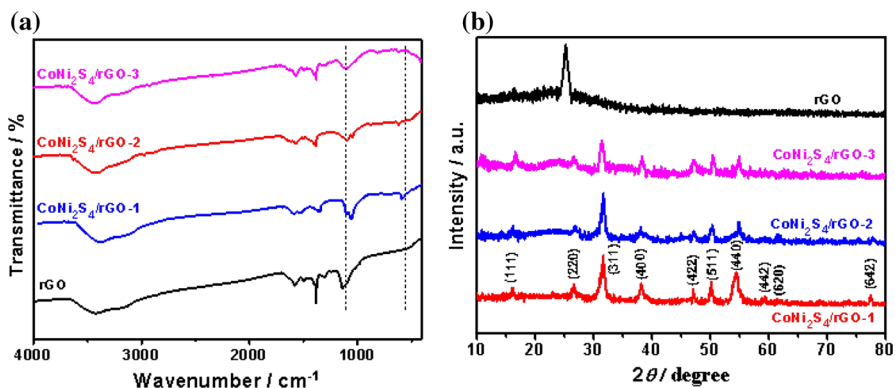Fig. 3 a FT-IR spectra and b XRD patterns of rGO, $CoNi_2S_4$/rGO-1, $CoNi_2S_4$/rGO-2 and $CoNi_2S_4$/rGO-3

(311), (400), (422), (511), (440), (442), (620) and (642) planes (JCPDS PDF#73-1297), respectively, demonstrate the successful formation of CoNi$_2$S$_4$. As can also be seen from the spectra, the more the addition of graphene, the weaker is the CoNi$_2$S$_4$ peak displayed in CoNi$_2$S$_4$/rGO. Moreover, the peak of rGO disappears in the CoNi$_2$S$_4$/rGO-1, CoNi$_2$S$_4$/rGO-2 and CoNi$_2$S$_4$/rGO-3 nanocomposites, which is because the introduction of CoNi$_2$S$_4$ weakened or avoided the overlap of rGO sheets, further reducing the graphitizing crystallization [33]. In addition, the absence of peaks of NiS$_2$, CoS$_2$ or CoNi$_2$O$_4$, indicate relatively purer CoNi$_2$O$_4$ generation.

Raman spectra were examined to analyze the structure of the samples. In Fig. 4a, two obvious primary graphitic peaks at about 1350 and 1588 cm^{-1} belong to the D and G bands, respectively. The D band arises from the imperfections of the rGO sheets, which is an indication of defects in the graphene, and the G band is because of the splitting of the E_{2g} in-plane vibrational mode of graphene, illustrating the sp^2 hybridization of C atoms in the rGO [21]. In addition, the I_D/I_G value denotes the degree of graphitization, the defects or the domain size of graphitization. Generally, the I_D/I_G value for amorphous carbon is about 1.0. The decreased I_D/I_G values suggest disordered carbon coupled with a partial graphite layer [34, 35]. Compared with rGO, the nanocomposites of CoNi$_2$S$_4$/rGO-1, CoNi$_2$S$_4$/rGO-2 and CoNi$_2$S$_4$/rGO-3 have higher values of I_D/I_G, implying more detects in the rGO sheets after combined with CoNi$_2$S$_4$. Several peaks recorded within the range in 200–700 cm^{-1} reveal a valid demonstration of typical Raman vibration modes for the metal-containing compound CoNi$_2$S$_4$ [28].

The TGA curves shown in Fig. 4b reflect the thermal stabilities of all the materials. For all the samples, the weight loss before 120 °C is due to the evaporation of the physical water adsorbed on the material surfaces. The weight loss at 120–730 °C is due to the thermal degradation of rGO; the mass degradation values are 15.5, 20.3 and 30.5% for CoNi$_2$S$_4$/rGO-3, CoNi$_2$S$_4$/rGO-2 and CoNi$_2$S$_4$/rGO-1, respectively, showing that CoNi$_2$S$_4$/rGO-2 and CoNi$_2$S$_4$/rGO-3 have relatively high thermallstability. As can clearly be seen, the almost complete lack of weight loss when the temperature is higher than 730 °C and the residual mass indicate the thermally stable CoNi$_2$S$_4$.
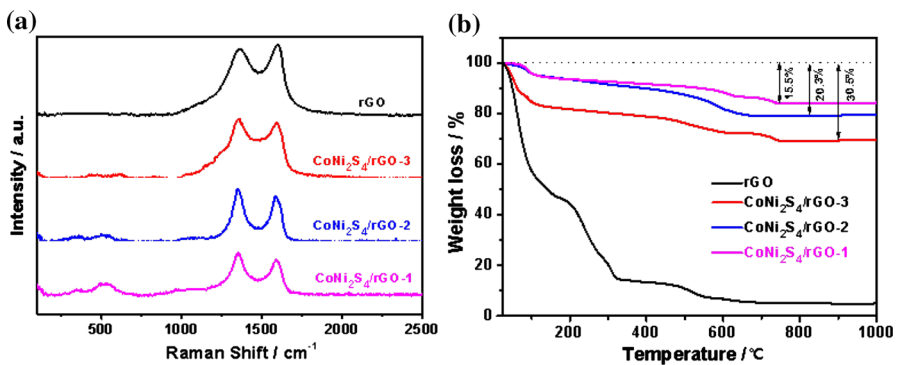

Fig. 4 a Raman spectra and b TGA curves of the rGO, CoNi$_2$S$_4$/rGO-1, CoNi$_2$S$_4$/rGO-2 and CoNi$_2$S$_4$/rGO-3

The N_2 adsorption–desorption isotherms of CoNi$_2$S$_4$/rGO-2 are explored in Fig. 5a for the specific surface area and pore size distribution. This curve exhibits a clear adsorption–desorption hysteresis loop, which is in accordance with a type IV isotherm on the basis of the IUPAC classification [36]. Moreover, as evaluated by the Barrett–Joyner–Halenda method, the pore sizes (inset of Fig. 5a) concentrate at 2.82 and 3.77 nm, indicating the mesoporous structure of CoNi$_2$S$_4$/rGO-2. The calculated specific Brunauer–Emmett–Teller surface (75.08 m^2 g^{-1}) and the mesoporous structure can together provide more active sites for the electrolyte and provide easy permeation to the mesoporous structure [37, 38].
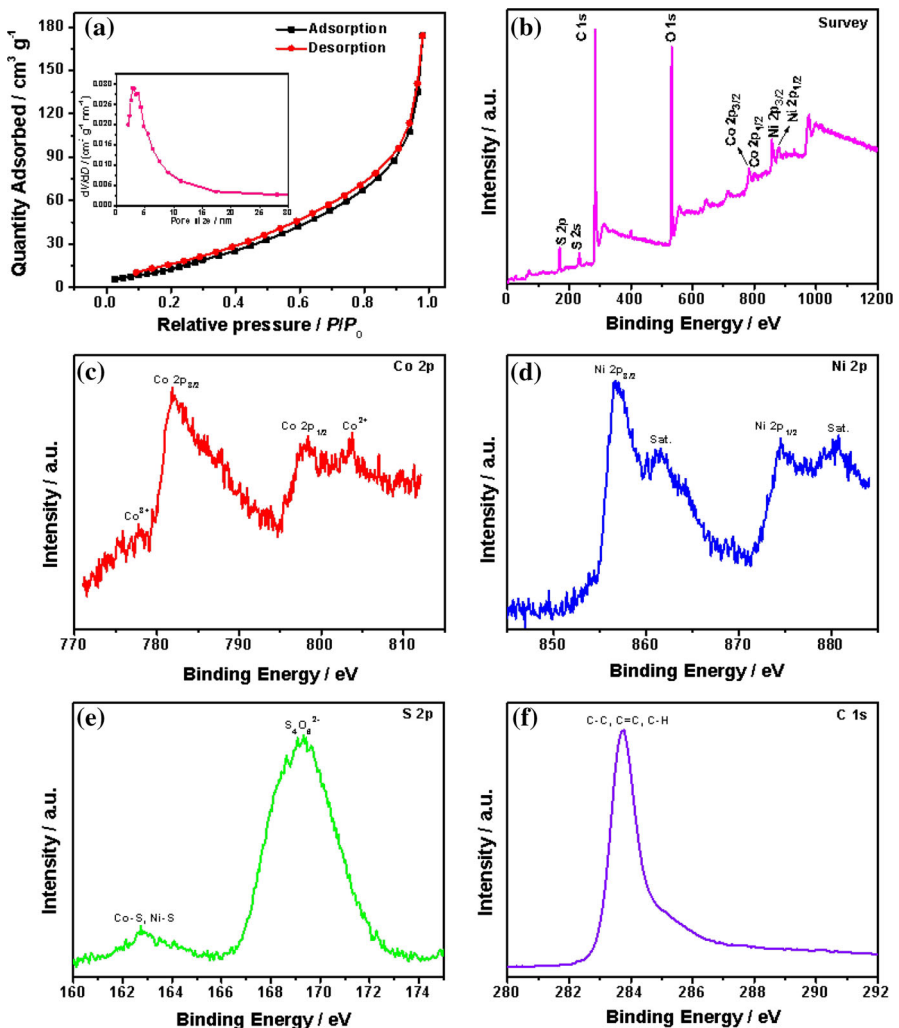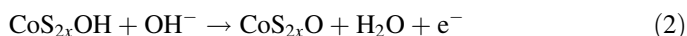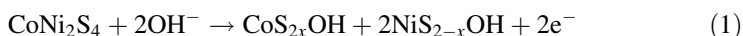

Fig. 5 **a** N_2 adsorption–desorption isotherms and pore size distributions of CoNi$_2$S$_4$/rGO-2; **b** XPS spectrum of the survey; **c** Co 2p; **d** Ni 2p; **e** S 2p; **f** C 1s

XPS was further investigated to analyze the elemental composition and chemical states of the CoNi$_2$S$_4$/rGO-2 nanocomposites, as shown in Fig. 5b–f and Fig. S3. The representative survey in Fig. 5b reveals the existence of Co, Ni, S, C and O elements. In the Co 2p spectrum of Fig. 5c, the peaks with binding energies around 781.92 and 798.29 eV can be well assigned to Co 2$p_{3/2}$ and Co 2$p_{1/2}$, respectively, and peaks at 777.83 and 803.45 eV can be attributed to Co^{3+} and Co^{2+}, respectively [39, 40]. With regard to the Ni 2p spectrum in Fig. 5d, the peaks at 856.71 and 861.52 eV are, respectively, Ni 2$p_{3/2}$ and its shake-up satellite peak, while the peaks located at 874.55 and 880.62 eV can be ascribed to Ni 2$p_{1/2}$ and its shake-up satellite peak, respectively. Furthermore, the two spin–orbit doublets and two shake-up satellites fit well with Ni^{2+} and Ni^{3+} [32, 41]. In the S 2p spectrum (Fig. 5e), the obvious peak centered on the binding energy of 169.29 eV is caused by the sulfur ions with a higher oxide state of S$_4$O$_6^{2-}$ at the surface due to the partial oxidation of CoNi$_2$S$_4$ [29, 32, 42], and the binding energy at 162.73 eV agrees with the metal-sulfur bonds (CO–S, Ni–S) in the ternary metal sulfides [40]. In the C 1s spectrum (Fig. 5f), the distinct peak at the binding energy of 287.82 eV can be traced back to the C–C, C=C and C–H bonds, which also illustrates the successful formation of honeycomb-like graphene [42, 43]. To evaluate the electrochemical performance in supercapacitors, the CV, GCD and EIS measurements were carried out in 2 M KOH electrolytes. Figure 6a exhibits CV curves of the CoNi$_2$S$_4$/rGO-1, CoNi$_2$S$_4$/rGO-2 and CoNi$_2$S$_4$/rGO-3 electrodes with the potential window at 0–0.55 V at a scan rate of 10 mV s^{-1}. Clearly, the CoNi$_2$S$_4$/rGO-2 material holds the largest integral area, indicating the maximum specific capacitance when compared with CoNi$_2$S$_4$/rGO-1 and CoNi$_2$S$_4$/rGO-2. All the nanocomposites take on distinct redox peaks rather than rectangular shapes, implying a pseudo-capacitance energy storage mechanism, which is dominated by CoNi$_2$S$_4$ through the reversible Faradaic redox reactions of Co^{2+}/Co^{3+}/Co^{4+} and Ni^{2+}/Ni^{3+} at the electrolyte/electrode interface by the following reactions [41]:

$$CoNi_2S_4 + 2OH^- \rightarrow CoS_{2x}OH + 2NiS_{2-x}OH + 2e^- \tag{1}$$

$$CoS_{2x}OH + OH^- \rightarrow CoS_{2x}O + H_2O + e^- \tag{2}$$

CV curves of the CoNi$_2$S$_4$/rGO-2 electrode at various scan rates from 5 to 100 mV s^{-1} are shown in Fig. 6b. As can be clearly seen, the anodic peak shifts into higher potentials and the corresponding cathodic peak shifts toward lower potentials as the scan rates increase, which indicates fast redox reactions and a relatively small resistance for this electrode material [39]. In addition, when the scan rate iis ncreased to 100 mV s^{-1}, the redox peaks can still maintain a distinct form, clearly indicating a good rate performance. Furthermore, the redox peak current and the square root of the scanning rate illustrates a linear correlation with the result in Fig. 6c, which is due to the fast redox reactions between the electrode and the electrolyte interface [44].

To further estimate the capacitive performance of the CoNi$_2$S$_4$/rGO-2 nanocomposite electrode, GCD measurements were conducted with the voltage window ranging from 0 to 0.47 V at a series of current densities from 0.5 to 10 A g^{-1}. As shown in Fig. 6d, the obtained GCD curves take on nonlinear profiles, which results
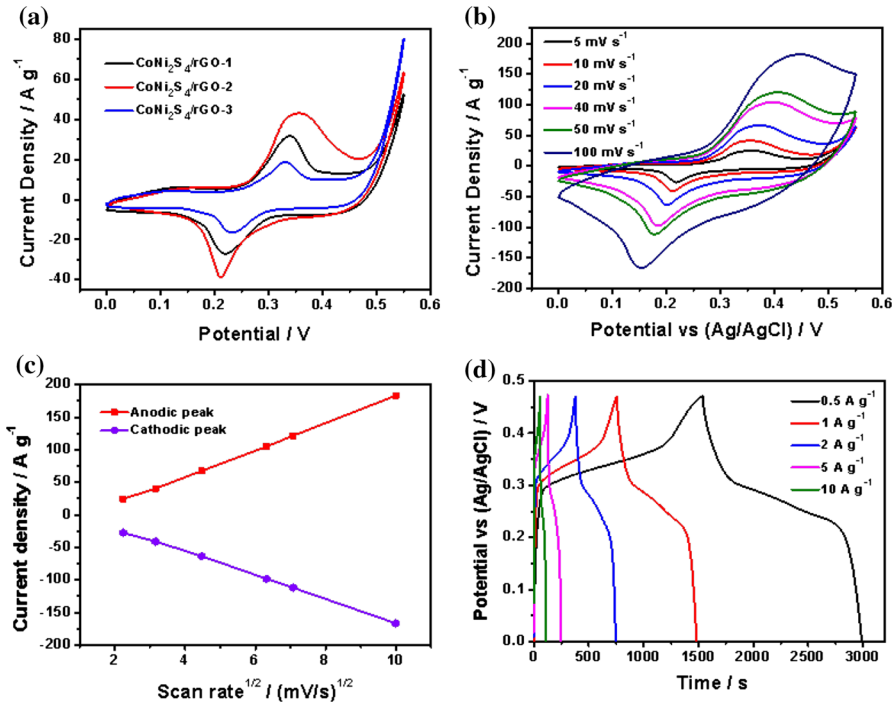
Fig. 6 Electrochemical performances: **a** CV curves of CoNi$_2$S$_4$/rGO-1, CoNi$_2$S$_4$/rGO-2 and CoNi$_2$S$_4$/rGO-3 electrodes at 10 mV s^{-1}; **b** CV curves of CoNi$_2$S$_4$/rGO-2 at various scan rates of 5, 10, 20, 40, 50 and 100 mV s^{-1}; **c** the linear relationship of the CoNi$_2$S$_4$/rGO-2 electrode between the anodic peak and the square root of various scan rates, and the cathodic peak and the square root of various scan rates; **d** GCD curves of the CoNi$_2$S$_4$/rGO-2 electrode at current densities of 0.5, 1, 2, 5 and 10 A g^{-1}

from the reversible redox reactions and demonstrates typical pseudocapacitive behavior, matching well with the CV curves in Fig. 6b. In addition, the symmetrical GCD curves hold good proof of the fast reversibility of the CoNi$_2$S$_4$/rGO-2 electrode material.

The specific capacitances can be obtained from the GCD curves and Eq. (3) [45]:

$$C_s = I \times \Delta t / (\Delta V \times m) \qquad (3)$$

where C_s, I, Δt and m are the specific capacitance (F g^{-1}), discharge current density (A g^{-1}), discharge time (s), potential window (V) during the charge–discharge process and the mass (g) of the active materials, respectively. The calculated specific capacitances of the CoNi$_2$S$_4$/rGO-1, CoNi$_2$S$_4$/rGO-2 and CoNi$_2$S$_4$/rGO-3 electrodes are shown in Fig. 7a. At a current density of 0.5 A g^{-1}, the specific capacitances of CoNi$_2$S$_4$/rGO-1, CoNi$_2$S$_4$/rGO-2 and CoNi$_2$S$_4$/rGO-3 are 1308, 1621 and 1216 F g^{-1}, respectively, proving the excellent electrochemical performance of CoNi$_2$S$_4$/rGO-2. In addition, the specific capacitances of CoNi$_2$S$_4$/rGO-2 electrode are 1539, 1466, 1321 and 1243 F g^{-1} at 1, 2, 5 and 10 A g^{-1}, respectively, and the specific capacitance retentions are calculated to be 56.04, 76.7 and 62.7% of CoNi$_2$S$_4$/rGO-1, CoNi$_2$S$_4$/rGO-2 and CoNi$_2$S$_4$/rGO-3, respectively, even at
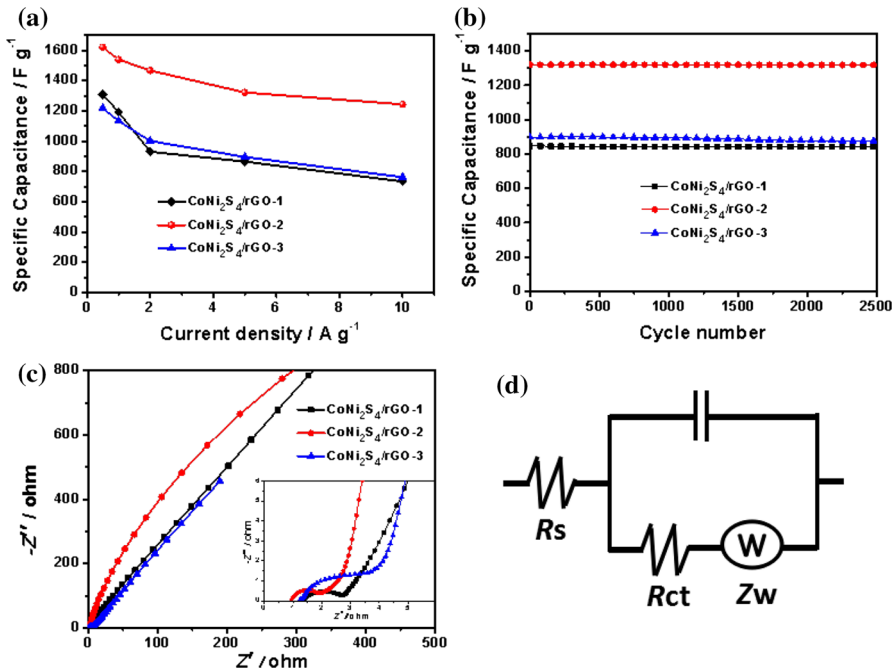
Fig. 7 **a** Specific capacitances with various discharge current densities; **b** cycle stability on the charge–discharge numbers measured at the current density of 10 A g^{-1}; **c** Nyquist plots for CoNi$_2$S$_4$/rGO-1, CoNi$_2$S$_4$/rGO-2 and CoNi$_2$S$_4$/rGO-3 electrodes; **d** equivalent circuit of the as-prepared CoNi$_2$S$_4$/rGO-2 electrode

10 A g^{-1}. It is well known that specific capacitances decay by degrees in pace with the increase of discharge current densities, and that this phenomenon can be interpreted as the diffusion and migration of electrolyte ions OH$^-$ being restricted because of the diffusion effect at higher current densities [39, 46].

The good supercapacitive behavior of the CoNi$_2$S$_4$/rGO nanocomposite can be explained as follows: (1) the well-coated CoNi$_2$S$_4$ nanoparticles in the rGO layers improved the electrical contact between the active materials and the electrolytes; (2) the aerogel structure offers more electroactive spots for electroactive ions and provides more efficient pathways for charge transfer [39, 47]; and (3) compared with Co–Ni oxide, CoNi$_2$S$_4$ exhibits good electrical conductivity.

As a key criterion of electrochemical characteristics for electrode materials, cycle stability tests were examined through repeated charge–discharge procedures. Figure 7b shows the cycle performances of the CoNi$_2$S$_4$/rGO-1, CoNi$_2$S$_4$/rGO-2 and CoNi$_2$S$_4$/rGO-3 electrodes at a current density of 5 A g^{-1}. It can clearly be seen that there is almost no capacitance loss for the CoNi$_2$S$_4$/rGO-2 material, and 97.2 and 98.8% capacitance retention for CoNi$_2$S$_4$/rGO-2 and CoNi$_2$S$_4$/rGO-3, respectively, after 2500 cycles, indicating excellent cycle stability. The good cycle stability for the materials may be attributed to their stable combination between CoNi$_2$S$_4$ and rGO. In addition, the good reversible redox reaction of CoNi$_2$S$_4$ can also ensure good cycling stability.

The EIS analysis was executed within the range of 0.01–100 kHz at an open-circuit potential with the amplitude of 5 mV for further research on the conductivity of the materials with the Nyquist plots shown in Fig. 7c and the corresponding equivalent circuit in Fig. 7d. The Nyquist plots include high-, low- and intermediate-frequency regions. All electrodes take on similar semi-circle arc shapes in the high-frequency region, implying charge-transfer resistance (Rct), which is controlled by reaction kinetics. Compared with the $CoNi_2S_4$/rGO-1 (1.32 Ω) and $CoNi_2S_4$/rGO-3 (2.33 Ω) electrodes, the Rct of $CoNi_2S_4$/rGO-2 (0.99 Ω) is smaller, which is consistent with this law: the larger the semicircle, the larger the Rct. The bulk resistances (Rs) were obtained by the intercept in the real part (Z') in the high-frequency region with their values of 1.37, 0.92 and 1.28 Ω for $CoNi_2S_4$/rGO-1, $CoNi_2S_4$/rGO-2 and $CoNi_2S_4$/rGO-3, respectively. This finding illustrates that the proper combination between $CoNi_2S_4$ and rGO could promote electroconductivity.

Resent research has shown that the two-electrode cell is more suitable than the three-electrode cell in simulating a packaged supercapacitor, which is because of the similar physical architecture and the charge transfer condition for the two-electrode cell and a packaged supercapacitor [48]. Therefore, an asymmetric two-electrode
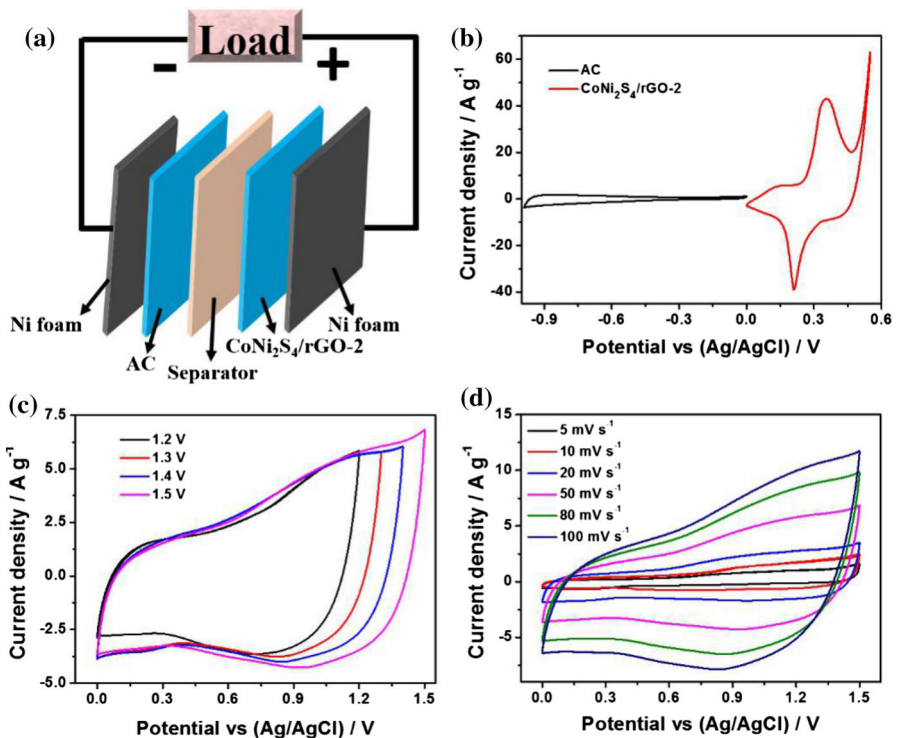

Fig. 8 **a** Diagram of the AC//$CoNi_2S_4$/rGO-2 asymmetric electrode device; **b** CV curves of AC and $CoNi_2S_4$/rGO-2 at 10 mV s^{-1}; **c** CV curves of the AC//$CoNi_2S_4$/rGO-2 asymmetric electrode at different voltage windows at the scan rate of 50 mV s^{-1}; **d** CV curves of AC//$CoNi_2S_4$/rGO-2 asymmetric supercapacitor at various scan rates of 5, 10, 20, 50, 80 and 100 mV s^{-1}

system has been assembled in Fig. 8a. To balance the charge in the positive and negative electrodes, the CoNi$_2$S$_4$/rGO-2 and AC masses were in accord with Eq. (4):

$$\frac{m_+}{m_-} = \frac{C_{s_-} \times \Delta V_-}{C_{s_+} \times \Delta V_+} \qquad (4)$$

where m represents the mass of the positive (m_+) or negative electroactive material (m_-), C represents the specific capacitance for the positive (C_{s+}) or negative material (C_{s-}), and (ΔV_-) represents the operating voltage window for positive (ΔV_+) or negative material (ΔV_-).

Figure 8b exhibits the CV curves at 10 mV s^{-1} of the CoNi$_2$S$_4$/rGO-2 from 0 to 0.55 V and AC from − 1 to 0 V, respectively. For the CoNi$_2$S$_4$/rGO-2 and AC, the specific capacitance were calculated as 1539 and 330 F g^{-1}, and, accordingly, the masses were 0.8 and 2.0 mg, respectively. From the CV curves of the CoNi$_2$S$_4$/rGO-2 asymmetric electrode at 50 mV s^{-1} in various voltage windows (Fig. 8c), the appropriate stable window was chosen as 0–1.5 V for further investigation. As can be seen from Fig. 8d, the asymmetric GCD curves take on a rectangular-like shape, representative of both the electrical double-layer capacitor and the pseudocapacitance capacitor.
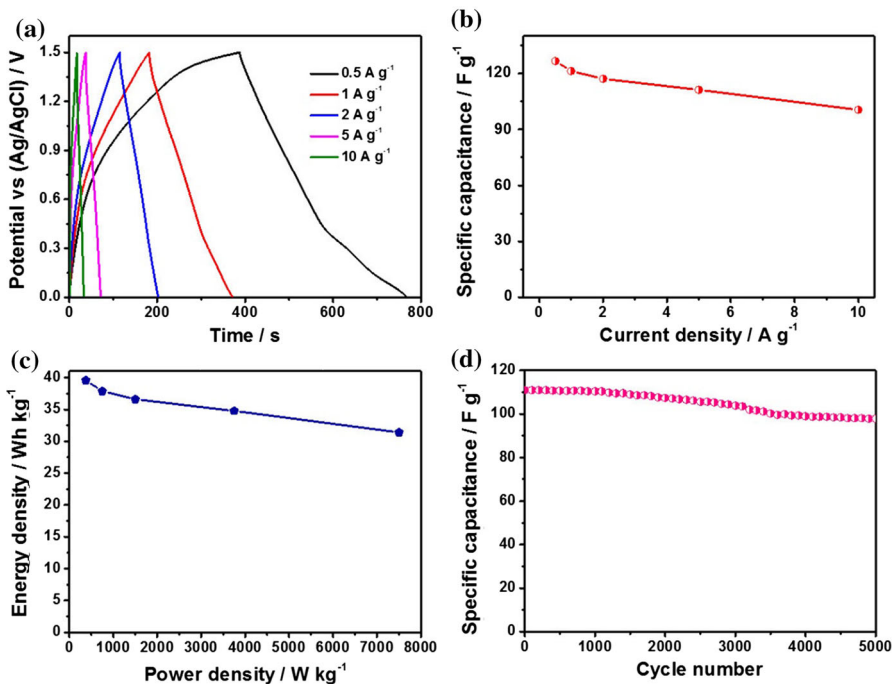

Fig. 9 The GCD curves (**a**) and corresponding specific capacitances (**b**) of the AC//CoNi$_2$S$_4$/rGO-2 asymmetric electrode at different current densities; **c** cycling stability of AC//CoNi$_2$S$_4$/rGO-2 asymmetric supercapacitor at a current density of 5 A g^{-1}; **d** Ragone plot of the AC//CoNi$_2$S$_4$/rGO-2 asymmetric supercapacitor

The GCD measurement was carried out at different current densities (Fig. 9a) and the obtained GCD curves take on sawtooth-like lines, which is attributed to the reversible Faraday reactions arising from the pseudocapacitive materials of $CoNi_2S_4$/rGO-2. In addition, the AC//$CoNi_2S_4$/rGO-2 asymmetric supercapacitor exhibited specific capacitances of 126.6, 121.2, 117.1, 111.2 and 100.5 F g^{-1} with current densities of 0.5, 1, 2, 5 and 10 A g^{-1}, respectively, having the high capacitance retention of 79.4%.

Promoting energy density has been studied very actively. A Ragone plot was fabricated (Fig. 9c) and the energy densities and power densities were received through GCD curves at various densities by Eqs. (5) and (6), respectively. According to the Ragone plot, the energy density possesses the highest value of 39.56 W h kg^{-1} at the power density of 374.8 W kg^{-1}.

$$E = \frac{1}{2} \times C_s \times (\Delta V)^2 \qquad (5)$$

$$P = \frac{E}{\Delta t} \qquad (6)$$

As a significant factor in investigating the practical application of asymmetric supercapacitors, the cycle stability was measured, as shown in Fig. 9d. After 5000 charge–discharge cycles at the current density of 5 A g^{-1}, the AC//$CoNi_2S_4$/rGO-2 asymmetric electrode demonstrated an outstanding cycle stability of 87.4% capacitance retention. All these electrochemical performances confirm the potential application of $CoNi_2S_4$/rGO materials for supercapacitors.

Conclusions

$CoNi_2S_4$/rGO nanocomposites with various amounts of graphene loading were prepared by a facile one-step solvothermal method. The well-coated $CoNi_2S_4$ nanoparticles in the rGO layers can improve the electrochemical performance of active materials. The electrodes possess excellent performances with high specific capacitance, good rate capability and outstanding cycling stability. In addition, the electrodes show high energy densities as asymmetric supercapacitors. Hence, the $CoNi_2S_4$/rGO nanocomposite materials are potential candidates for energy storage applications.

References

1. P. Simon, Y. Gogotsi, Nat. Mater. **7**, 845 (2008)
2. X. Wei, X. Jiang, J. Wei, S. Gao, Chem. Mater. **28**, 445 (2016)
3. L. Wang, Y. Shao, J. Zhang, M. Anpo, Res. Chem. Intermed. **34**, 267 (2008)
4. Y. Liu, L. Wang, J. Zhang, F. Chen, M. Anpo, Res. Chem. Intermed. **37**, 949 (2011)
5. F. Zhang, T. Zhang, X. Yang, L. Zhang, K. Leng, Y. Huang, Energ. Environ. Sci. **6**, 1623 (2013)
6. Y. Jiang, X. Cui, L. Zu, Z. Hu, J. Gan, J. Nanosci. Nanotechno. **17**, 507 (2017)
7. M. Winter, R.J. Brodd, Cheminform **35**, 4245 (2004)
8. D.P. Dubal, N.R. Chodankar, Z. Caban-Huertas, F. Wolfart, M. Vidotti, R. Holze, C.D. Lokhande, J. Power Sourc. **308**, 158 (2016)
9. J. Yu, J. Wu, H. Wang, A. Zhou, C. Huang, H. Bai, L. Li, A.C.S. Appl, Mater. Inter. **8**, 4724 (2016)
10. B. Dong, X. Zhang, X. Xu, G. Gao, S. Ding, J. Li, B. Li, Carbon **80**, 222 (2014)
11. G. Godillot, P.L. Taberna, B. Daffos, P. Simon, C. Delmas, L. Guerlou-Demourgues, J. Power Sour. **331**, 277 (2016)
12. B. Li, F. Dai, Q. Xiao, L. Yang, J. Shen, C. Zhang, M. Cai, Energ. Environ. Sci. **9**, 102 (2015)
13. F. Miao, C. Shao, X. Li, K. Wang, Y. Liu, J. Mater. Chem. A **4**, 4180 (2016)
14. C. Ma, J. Sheng, C. Ma, R. Wang, J. Liu, Z. Xie, J. Shi, Chem. Eng. J. **304**, 587 (2016)
15. L. Wei, M. Sevilla, A.B. Fuertes, R. Mokaya, G. Yushin, Adv. Energy Mater. **1**, 356 (2011)
16. M. Oschatz, S. Boukhalfa, W. Nickel, J.P. Hofmann, C. Fischer, G. Yushin, S. Kaskel, Carbon **113**, 283 (2017)
17. F. Yang, H. Yang, B. Tian, J. Zhang, D. He, Res. Chem. Intermed. **39**, 1685 (2013)
18. S. Li, D. Wu, C. Cheng, J. Wang, F. Zhang, Y. Su, Angew. Chem. **52**, 12105 (2013)
19. H. Li, L. Wang, Y. Liu, J. Lei, J. Zhang, Res. Chem. Intermed. **42**, 3979 (2016)
20. W. Ma, S. Chen, S. Yang, W. Chen, W. Weng, Y. Cheng, M. Zhu, Carbon **113**, 151 (2017)
21. X. Yan, K. Gan, B. Tian, J. Zhang, L. Wang, D. Lu, Res. Chem. Intermed. **44**, 1 (2018)
22. N. Li, K. Gan, D. Lu, J. Zhang, L. Wang, Res. Chem. Intermed. **44**, 1105 (2018)
23. M. Li, Z. Mei, J. Yu, H. Cheng, Q. Li, Small **13**, 1602994 (2017)
24. L. Bao, T. Li, S. Chen, C. Peng, L. Li, Q. Xu, Y. Chen, E. Ou, W. Xu, Small **13**, 1602077 (2017)
25. Z. Wu, Y. Zhu, X. Ji, J. Mater. Chem. A **2**, 14759 (2014)
26. Y. Johnbosco, V. Elumalai, M. Bhagavathiachari, A.S. Samuel, E. Elaiyappillai, P.M. Johnson, J. Electroanal. Chem. **797**, 78 (2017)
27. Z. Ai, Z. Hu, Y. Liu, M. Yao, ChemPlusChem **81**, 322 (2016)
28. J. Shen, J. Wu, L. Pei, M.T.F. Rodrigues, Z.Q. Zhang, F. Zhang, X. Zhang, P.M. Ajayan, M. Ye, Adv. Energy Mater. **6**, 314 (2016)
29. J. Zhao, Z. Li, M. Zhang, A. Meng, Q. Li, J. Power Sour. **332**, 355 (2016)
30. J. Shen, X. Xu, P. Dong, Z. Zhang, R. Baines, J. Ji, Y. Pei, M. Ye, Ceram. Int. **42**, 8120 (2016)
31. S. Liu, J. Xie, C. Fang, G. Cao, T. Zhu, X. Zhao, J. Mater. Chem. **22**, 19738 (2012)
32. J. Tang, J. Shen, N. Li, M. Ye, Ceram. Int. **41**, 6203 (2015)
33. W.S.H. Jr, R.E. Offeman, J. Am. Chem. Soc. **80**, 1339 (1958)
34. M. Liu, X. Ma, L. Gan, J. Mater. Chem. A **2**, 17107 (2014)
35. L. Miao, D. Zhu, Y. Zhao, Micropor. Mesopor. Mat. **253**, 1 (2017)
36. K. Kailasam, A. Fischer, G. Zhang, J. Zhang, M. Schwarze, M. Schröder, X. Wang, R. Schomäcker, A. Thomas, Chemsuschem **8**, 1404 (2015)
37. X. Wang, Y. Lin, Y. Su, B. Zhang, C. Li, H. Wang, L. Wang, Electrochim. Acta **225**, 263 (2017)
38. M. Qorbani, N. Naseri, A.Z. Moshfegh, A.C.S. Appl, Mater. Inter. **7**, 11172 (1944)
39. C. Yuan, J. Li, L. Hou, X. Zhang, L. Shen, X.W. Lou, Adv. Funct. Mater. **22**, 4592 (2012)
40. J. Pu, T. Wang, H. Wang, Y. Tong, C. Lu, W. Kong, Z. Wang, ChemPlusChem **79**, 577 (2014)
41. L. Mei, T. Yang, C. Xu, Nano Energy **3**, 36 (2014)
42. J. Yang, C. Yu, X. Fan, S. Liang, S. Li, H. Huang, Z. Ling, C. Hao, J. Qiu, Energ. Environ. Sci. **9**, 1299 (2016)
43. L.G. Beka, X. Li, X. Xia, W. Liu, Diam. Relat. Mater. **73**, 169 (2017)
44. H. Chen, Y. Ai, F. Liu, X. Chang, Y. Xue, Q. Huang, C. Wang, H. Lin, S. Han, Electrochim. Acta **213**, 55 (2016)
45. S. Zhang, D. Li, S. Chen, X. Yang, X. Zhao, Q. Zhao, S. Komarneni, D. Yang, J. Mater. Chem. A **5**, 12453 (2017)

46. B. Liu, B. Liu, Q. Wang, X. Wang, Q. Xiang, D. Chen, G. Shen, A.C.S. Appl, Mater. Inter. **5**, 10011 (2013)
47. G. Zhang, X.W. Lou, Adv. Mater. **25**, 976 (2013)
48. R.B. Rakhi, W. Chen, D. Cha, H.N. Alshareef, Nano Lett. **12**, 2559 (2012)